Nanoscale Advances

ROYAL SOCIETY OF CHEMISTRY

PAPER

View Article Online
View Journal | View Issue

Check for updates

Cite this: *Nanoscale Adv.*, 2026, **8**, 1409

Received 7th October 2025
Accepted 30th December 2025

DOI: 10.1039/d5na00946d

rsc.li/nanoscale-advances

Synergistic enhancement of the hydrogen evolution reaction by bimetallic Pt–Ru nanoparticles supported on a carbon xerogel

Abdalla Abdelwahab,[a] Jamal R. Humaidi,[a] Fahad Abdulaziz,[a] Abdulaziz Alanazi,[b] Khalaf M. Alenezi[a] and Ahmed A. Farghali*[c]

Pt–Ru alloys have shown promising catalytic activity toward the hydrogen evolution reaction (HER) in acidic media; however, their stability remains a critical challenge due to the oxidation and dissolution of Ru species in 0.5 M H_2SO_4. Herein, the synthesis and comparative assessment of a series of electrocatalysts based on a carbon xerogel loaded with platinum and ruthenium, Pt–Ru, specifically a pure carbon xerogel (CX), 5 wt% platinum-loaded CX (Pt5/CX), 5 wt% platinum and 2.5 wt% ruthenium co-loaded CX (Pt5:Ru2.5/CX), and 5 wt% platinum and 5 wt% ruthenium co-loaded CX (Pt5:Ru5/CX) were evaluated for the HER. The carbon xerogel served as a high-surface-area, porous, and conductive substrate, promoting uniform distribution of the metallic nanoparticles, mitigating Ru leaching, and improving charge transfer during the HER. The Pt5:Ru2.5/CX composite displayed superior catalytic activity, achieving the lowest overpotential (39 mV, at 10 mA cm^{-2}), minimal Tafel slope (29 mV dec^{-1}), and maximal double-layer capacitance (C_{dl} of 52.68 mF cm^{-2}) in 0.5 M H_2SO_4. The improved HER activity is ascribed to the synergistic interaction between Pt and Ru, together with reduced charge transfer resistance (R_{ct}, 0.4 Ω) and active site accessibility afforded by the carbon xerogel matrix.

1. Introduction

The worldwide shift to sustainable and renewable energy sources has increased the need for clean fuels, with hydrogen (H_2) emerging as a viable energy carrier due to its high energy density and ecologically friendly combustion byproduct – which is water.[1] Among diverse hydrogen generation processes, water electrolysis is distinguished as a clean and scalable method, especially when fueled by renewable energy sources like solar or wind.[2] The practical implementation of water electrolysis is significantly limited by the slow kinetics and elevated overpotentials of the hydrogen evolution reaction (HER), particularly in acidic environments.[3] To address these restrictions, the creation of efficient, stable, and economical electrocatalysts is essential.

At present, platinum (Pt)-based materials are considered the standard electrocatalysts for the hydrogen evolution reaction (HER) owing to their negligible overpotential and superior catalytic performance.[4] Nonetheless, the elevated expense and limited availability of Pt considerably obstruct its extensive application in industrial electrolyzers. Consequently, substantial number of studies have concentrated on minimizing platinum usage through alloying with other transition metals or spreading it on high-surface-area conductive supports to boost its utilization efficiency.[5] The development of Pt-based bimetallic catalysts supported on porous carbonaceous matrices has garnered considerable attention among diverse techniques. These combinations can augment catalytic efficiency through synergistic effects, enhanced electrochemical surface area (ECSA), and improved charge transfer kinetics.[6]

Carbon xerogels (CXs), a kind of porous carbon material produced from the sol–gel polymerization of resorcinol and formaldehyde, have garnered significant interest as catalyst supports owing to their distinctive physicochemical characteristics.[7,8] These materials demonstrate a three-dimensional interconnected porous structure, substantial surface area, adjustable pore size distribution, and superior electrical conductivity. The customized porosity and surface chemistry of CX enable uniform distribution of metal nanoparticles and enhance effective mass transport and charge transfer in electrochemical processes. Furthermore, the surface of CX may be easily altered to immobilize active species and improve metal–support interactions, rendering them optimal platforms for electrocatalyst advancement.[9] The interaction between metal species and oxygen-containing functional groups on the carbon surface promotes metal retention and changes the

---

[a] *Department of Chemistry, College of Sciences, University of Hail, Ha'il, 81451, Saudi Arabia. E-mail: a.abdelsalam@uoh.edu.sa*

[b] *Department of Chemistry, College of Science and Humanities in Al-Kharj, Prince Sattam bin Abdulaziz University, Al-Kharj 11942, Saudi Arabia*

[c] *Materials Science and Nanotechnology Department, Faculty of Postgraduate Studies for Advanced Sciences, Beni-Suef University, 62511, Beni-Suef, Egypt. E-mail: aabdelwahab@psas.bsu.edu.eg; farghali@psas.bsu.edu.eg*

electronic structure of the catalyst, potentially modifying its catalytic performance.

Recent studies have extensively explored the amalgamation of Pt with other transition metals, like Ru, Ni, or Co, to enhance the HER efficacy while minimizing Pt usage. Ruthenium (Ru) has demonstrated significant potential as a co-catalyst due to its analogous hydrogen binding energy (HBE) to platinum, together with its greater availability and reduced cost. The integration of Ru into Pt-based systems can elicit electronic and geometric alterations that optimize hydrogen adsorption and desorption, improve d-band center alignment, and foster a bifunctional process wherein Ru aids in water dissociation and Pt enhances hydrogen evolution. These synergistic effects frequently result in augmented catalytic activity, increased durability, and superior resistance to poisoning intermediates. For example, Lei Zhang *et al.* reported the successful synthesis of Pt–Ru dimers in the form of single atom catalysts where the Pt–Ru dimers show more than 50 times higher HER activity than commercial Pt/C.[10] Unfortunately, Ru-based electrocatalysts often suffer from limited stability, primarily due to the oxidation and dissolution of Ru species, particularly under strongly acidic conditions such as 0.5 M H_2SO_4. One potential solution to this problem is the incorporation of Pt and/or Ru into a three-dimensional carbon matrix, which enhances electronic transport and suppresses the dissolution of the metal species into the electrolyte, thereby significantly improving the overall stability of the electrode.[11] For instance, Panpan Su *et al.* reported higher HER activity for Ru nanoparticles dispersed on O-doped graphene decorated with single metal atoms of Fe, Co, or Ni.[12] Moreover, L. Liu *et al.* reported the successful incorporation of Ru–Ru_2P into P-doped graphene which enhances the material stability for 125 h of operation.[13]

Although there are many publications on Pt–Ru alloys and their efficacy in the hydrogen evolution reaction (HER), the comprehensive examination of their performance when supported on carbon xerogels is still insufficiently investigated. This study involved the design and synthesis of a variety of nanostructured electrocatalysts consisting of carbon xerogels loaded with varying contents of platinum and ruthenium. So, a carbon xerogel (CX), 5 wt% platinum-loaded CX (Pt5/CX), 5 wt% platinum and 2.5 wt% ruthenium co-loaded CX (Pt5:Ru2.5/CX), and 5 wt% platinum and 5 wt% ruthenium co-loaded CX (Pt5:Ru5/CX) were synthesized and investigated for their HER activity. The objective was to assess the impact of Ru inclusion on the HER activity of Pt-based electrocatalysts and to determine an ideal composition that harmonizes catalytic performance with noble metal content.

The synthesized materials were characterized through various physicochemical and electrochemical techniques, including scanning electron microscopy (SEM), X-ray photoelectron spectroscopy (XPS), and X-ray diffraction (XRD), to evaluate their structural, morphological, and compositional attributes. The electrochemical HER performance was assessed in an acidic electrolyte (0.5 M H_2SO_4) employing linear sweep voltammetry (LSV), Tafel analysis, electrochemical impedance spectroscopy (EIS), and cyclic voltammetry (CV) to ascertain critical parameters including overpotential, Tafel slope, charge transfer resistance, and double-layer capacitance (C_{dl}) as a measure of electrochemically active surface area.

2. Experimental section

2.1 Materials

Resorcinol (99%), formaldehyde solution (37 wt%), sodium carbonate (Na_2CO_3), chloroplatinic acid hexahydrate ($H_2PtCl_6\cdot 6H_2O$), ruthenium(III) chloride hydrate ($RuCl_3\cdot xH_2O$), and 5 wt% Nafion solution were acquired from Merck. Ethanol and all other chemicals were of analytical grade and utilized without additional purification. Deionized (DI) water was utilized in all experimental procedures.

2.2 Synthesis of the carbon xerogel

Carbon xerogel (CX) was made through the polymerization of resorcinol and formaldehyde, employing sodium carbonate as a catalyst.[14] In a standard procedure, calculated amounts of resorcinol and formaldehyde with a molar ratio of 1 : 2 were mixed together until a clear solution was obtained. Subsequently, the calculated amounts of Na_2CO_3 and DI water were added where the molar ratio between resorcinol and catalyst was 200 : 1, and that between resorcinol and water was 1 : 17. The resultant solution was agitated for 30 minutes and transferred into a sealed Teflon-lined stainless steel autoclave, and subsequently underwent gelation and curing at 80 °C for 3 days. After curing, the resultant hydrogel was dried in a domestic microwave to yield the organic xerogel. The xerogel was carbonized in a nitrogen environment at 900 °C for 2 hours, with a heating rate of 5 °C min^{-1}, resulting in a carbon xerogel (CX).

2.3 Synthesis of the platinum-loaded carbon xerogel

Pt5/CX was synthesized *via* a hydrothermal method with some modifications to the reported one.[15] 200 mg of the previously synthesized CX was dispersed in 30 mL of ethanol *via* ultrasonication for 30 minutes. 26.5 mg of $H_2PtCl_6\cdot 6H_2O$, equating to 5 wt% Pt in relation to the CX mass, was dissolved in 30 mL DI water, and then added to the CX solution. The resultant mixture was placed in a 100 mL Teflon-lined stainless steel autoclave and underwent hydrothermal treatment at 180 °C for 12 h. Upon cooling to ambient temperature, the black solid product was obtained *via* centrifugation, subsequently washed three times with ethanol and deionized water to eliminate any unbound precursor, and finally dried at 80 °C under vacuum conditions. The dried powder was subsequently annealed at 300 °C for 2 hours in a nitrogen environment to enhance metal nanoparticle dispersion and convert the platinum precursor to metallic Pt. The synthesized catalyst was denoted as Pt5/CX.

2.4 Synthesis of Pt–Ru co-loaded carbon xerogels

Bimetallic Pt–Ru catalysts with two Ru contents (2.5% and 5%) were loaded on a carbon xerogel and synthesized by the same preparation procedure of Pt5/CX. A one-step hydrothermal process utilized chloroplatinic acid ($H_2PtCl_6\cdot 6H_2O$) and ruthenium(III) chloride hydrate ($RuCl_3\cdot xH_2O$) as metal precursors.

In a standard synthesis, 200 mg of carbon xerogel was suspended in 30 mL of ethanol using ultrasonication for 30 minutes. The suitable quantities of $H_2PtCl_6 \cdot 6H_2O$ and $RuCl_3 \cdot xH_2O$ were dissolved in 30 mL deionized water and after complete dissolution this was added to the CX and stirred for another 30 minutes. The same procedure of Pt5/CX was followed and the resultant materials were denoted as Pt5:Ru2.5/CX and Pt5:Ru5/CX, respectively.

2.5 Characterization techniques

To reveal the required information about the structure and morphology of the prepared materials, a variety of characterization techniques were used including X-ray diffraction (XRD) which was performed using a PANalytical Empyrean diffractometer, Netherlands. The diffractometer was equipped with Cu Kα radiation (λ = 1.5406 Å). XRD was utilized in order to determine the crystallinity and phase identification of the prepared materials. Moreover, field-emission scanning electron microscopy (FE-SEM) was used to determine the materials' morphology using a FEI-Quanta FEG-250 SEM, Switzerland. The microstructure and metal dispersion were characterized using high-resolution transmission electron microscopy (HRTEM, JEOL JEM 2100, Tokyo, Japan). The elemental composition and the oxidation states of the targeted elements were analyzed using X-ray photoelectron spectroscopy (XPS); Model Thermo Fisher Scientific spectrometer, USA.

2.6 Electrode preparation and electrochemical measurements

The electrochemical activity of the catalysts for the HER was assessed utilizing a typical three-electrode setup in a 0.5 M H_2SO_4 electrolyte at ambient temperature. A glassy carbon electrode (GCE, 5 mm diameter) served as the working electrode, a saturated Ag/AgCl electrode served as the reference electrode, and a graphite rod acted as the counter electrode. To fabricate the working electrode, 5 mg of the catalyst was suspended in a mixture of 400 μL of isopropanol along with 10 μL of 5 wt% Nafion solution. The combination underwent ultrasonication for 30 minutes to achieve a homogeneous ink. Subsequently, 10 μL of the ink was deposited over the polished GCE surface and allowed to dry at ambient temperature. For comparison, a commercial pure platinum electrode with a diameter of 3 mm was used.

Electrochemical experiments were performed on a Metrohm electrochemical workstation (Model PGSTAT128N). All potentials were adjusted to the reversible hydrogen electrode (RHE) utilizing the following equation:[16]

$$E_{\mathrm{RHE}} = E_{\mathrm{Ag/AgCl}} + 0.1976 + 0.059 \times \mathrm{pH}$$

Here, $E_{\mathrm{Ag/AgCl}}$ and E_{RHE} are the measured potentials against Ag/AgCl and RHE, respectively, and the pH equals 0.3 which is the pH of the electrolyte (0.5 M H_2SO_4).

The double-layer capacitance (C_{dl}) was obtained through cyclic voltammetry (CV) in the non-faradaic potential region at different scan rates from 5 to 100 mV s^{-1}. The electrochemically active surface area (ECSA) reflects the electrochemically accessible active sites under realistic operating conditions; this is more relevant to electrocatalytic performance than the total physical surface area obtained from BET analysis. Thus, the ECSA of the prepared electrodes was calculated using the C_{dl} values from the following relation:

$$\mathrm{ECSA} = \frac{C_{\mathrm{dl}}}{C_{\mathrm{s}}}$$

where C_{s} is the specific capacitance of a smooth surface in an acidic medium which is approximated as 0.040 mF cm^{-2}.[17] Moreover, electrochemical impedance spectroscopy (EIS) was conducted in the frequency range from 100 kHz to 0.1 Hz at an amplitude of 5 mV. The electrodes' long-term stability was evaluated using repetitive LSV at a scan rate of 20 mV s^{-1} for 24 h and chronopotentiometry (CP) at an applied constant current density of 10 mA cm^{-2} for 15 h.

Tafel slopes were derived from the linear sweep voltammetry (LSV) polarization curves at a scan rate of 5 mV s^{-1} by graphing overpotential (η) against the logarithm of current density ($\log j$) according to the following equation:[16]

$$\eta = a + b \log J$$

where "η" refers to the overpotential, "a" represents the Tafel constant, "b" is the Tafel slope, and "J" indicates current density.

The turnover frequency (TOF) was determined using the following equation:[16]

$$\mathrm{TOF} = \frac{j}{2 \times F \times n}$$

where j represents the current (A), and F and n are the Faraday constant and the number of moles of active sites.

3. Results and discussion

3.1 Physicochemical properties

3.1.1 XRD. X-ray diffraction (XRD) patterns were obtained to examine the crystalline structure and phase composition of the synthesized materials, as seen in Fig. 1. The carbon xerogel (CX) had diffraction peaks centered at 2θ values of 23° and 43°, indicative of the (002) and (101) planes of disordered graphitic carbon.[18] This extensive and low-intensity peak signifies the amorphous or turbostratic characteristics of the carbon framework. The integration of platinum into CX and Pt5/CX resulted in an XRD pattern exhibiting supplementary diffraction peaks at about $2\theta = 39.6°$, 46.2°, and 68.0° corresponding to the (111), (200), and (220) planes of face-centered cubic (FCC) metallic platinum (JCPDS No. 04-0802).[19] The presence of these peaks validates the effective synthesis of crystalline Pt nanoparticles. The (111) peak exhibits the highest intensity, indicating preferential orientation or predominant crystal formation along this plane.

The XRD patterns of the Pt5:Ru2.5/CX and Pt5:Ru5/CX samples, shown in Fig. 1, exhibited analogous diffraction characteristics to those of Pt5/CX, with peaks indicative of fcc

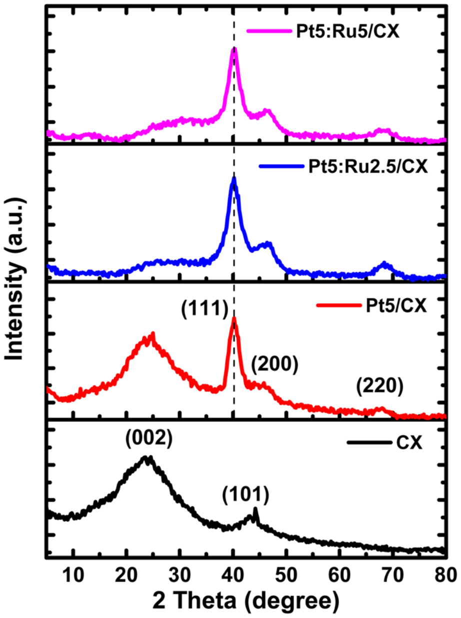

Fig. 1 X-ray diffraction (XRD) patterns of CX, Pt5/CX, Pt5:Ru2.5/CX, and Pt5:Ru5/CX samples.

Pt. No discernible diffraction peaks corresponding to crystalline Ru or RuO_2 were detected. This absence may be ascribed to the extremely scattered or amorphous characteristics of Ru species, or their integration into the Pt lattice, resulting in a Pt–Ru solid solution, which generally leads to peak shifting or broadening.[20] In both bimetallic samples, a minor displacement of the Pt(111) peak towards elevated 2θ values was noted in comparison to Pt5/CX, suggesting potential lattice contraction resulting from the partial substitution of Pt atoms by the smaller Ru atoms (atomic radius of Ru $\approx$ 1.34 Å *vs.* Pt $\approx$ 1.39 Å). This lattice distortion facilitates the creation of a Pt–Ru alloy at the nanoscale, potentially affecting the electrical structure and augmenting catalytic activity *via* synergistic effects.

3.1.2 Morphology characterization. FESEM analysis was performed to investigate the surface morphology of the synthesized materials, as shown in Fig. 2a–d. Fig. 2a displays the FESEM image of CX where a highly porous, sponge-like structure consisting of linked carbon spheres is shown. This three-dimensional porous network is characteristic of carbon xerogels formed from resorcinol–formaldehyde.[21] The homogeneous pore structure and elevated surface area of the CX matrix offer numerous anchoring sites and advantageous paths for electron and mass transport which are crucial for electrocatalytic applications. Upon loading with 5 wt% Pt, as shown in Fig. 2b, the surface of Pt5/CX preserved the general porous architecture of the parent xerogel, exhibiting heterogeneous aggregated structures of Pt dispersed throughout the carbon matrix.

The surface morphology of Pt5:Ru2.5/CX, shown in Fig. 2c shows different morphologies for Pt and Ru in the form of tiny, dispersed nanoparticles, exhibiting uniformly distributed metal nanoparticles on the porous carbon substrate. The particle size seemed somewhat reduced and exhibited a more uniform distribution compared to the monometallic Pt system. The enhancement in dispersion is due to the simultaneous introduction of Ru, which may affect nucleation and growth dynamics during the hydrothermal process.[10,22] The coexistence of both metals likely facilitated the development of bimetallic Pt–Ru nanoparticles or clusters that are more intricately linked with the carbon support. The FESEM image of the Pt5:Ru5/CX catalyst, shown in Fig. 2d, revealed a somewhat denser distribution of metal nanoparticles on the xerogel surface. Although the porous network remained intact, regional clustering of nanoparticles was noted with elevated Ru loading, potentially resulting from partial aggregation or coalescence during hydrothermal treatment or subsequent annealing. Nonetheless, the overall morphology remained advantageous for electrocatalysis, preserving the linked porosity and nanoscale characteristics crucial for promoting electrolyte infiltration and optimal exposure of active areas. The FESEM observations collectively affirm that the hydrothermal technique facilitates uniform distribution of metal nanoparticles on the CX support, and that Ru inclusion affects both particle dispersion and surface morphology. The meticulously maintained porous architecture and optimal distribution of Pt–Ru nanoparticles are anticipated to significantly contribute to the observed improvement in HER activity.

The HRTEM images reveal distinct morphological differences among the three catalysts, as shown in Fig. 2e–g. For Pt5/CX, as shown in Fig. 2e, the platinum nanoparticles appear in slice-like, aggregated domains, which suggests limited contact and poor dispersion with the carbon xerogel substrate. Upon partial incorporation of Ru (Pt5:Ru2.5/CX), as shown in Fig. 2f, the nanoparticles become more finely dispersed with reduced aggregation, indicating homogeneous dispersion of Pt and Ru. At higher Ru content (Pt5:Ru5/CX), as shown in Fig. 2g, the particles are smaller and uniformly distributed across the carbon xerogel framework, and exhibit clear alloyed structures, demonstrating that Ru effectively suppresses Pt aggregation and promotes stronger metal–support interactions. These observations suggest a progressive improvement in nanoparticle dispersion and alloy formation with increasing Ru content, which is expected to enhance the electroactive surface area and catalytic performance compared to Pt-only systems.

3.1.3 XPS. XPS analysis was conducted to examine the surface chemical composition and bonding environments of carbon in the produced catalysts. The deconvoluted C 1s and O 1s spectra of CX, Pt5/CX, Pt5:Ru2.5/CX, and Pt5:Ru5/CX are presented in Fig. 3, with the associated binding energies detailed in Table 1. The C 1s spectra of the CX, shown in Fig. 3a, displayed three deconvoluted peaks at around 284.00 eV, 285.07 eV, and 288.4 eV, which correspond to graphitic carbon with sp^2 hybridization (C–C/C=C), C–O/C–OH, and O–C=O, respectively.[23] The peaks indicate the partial oxidation of the carbon xerogel surface during synthesis and verify the existence of surface functional groups that facilitate the attachment of metal nanoparticles during hydrothermal treatment.

In Fig. 3b showing the C 1s spectra of Pt5/CX, analogous peak assignments were noted at 284.43, 285.09, and 288.34 eV, suggesting that the graphitic and oxygenated carbon species

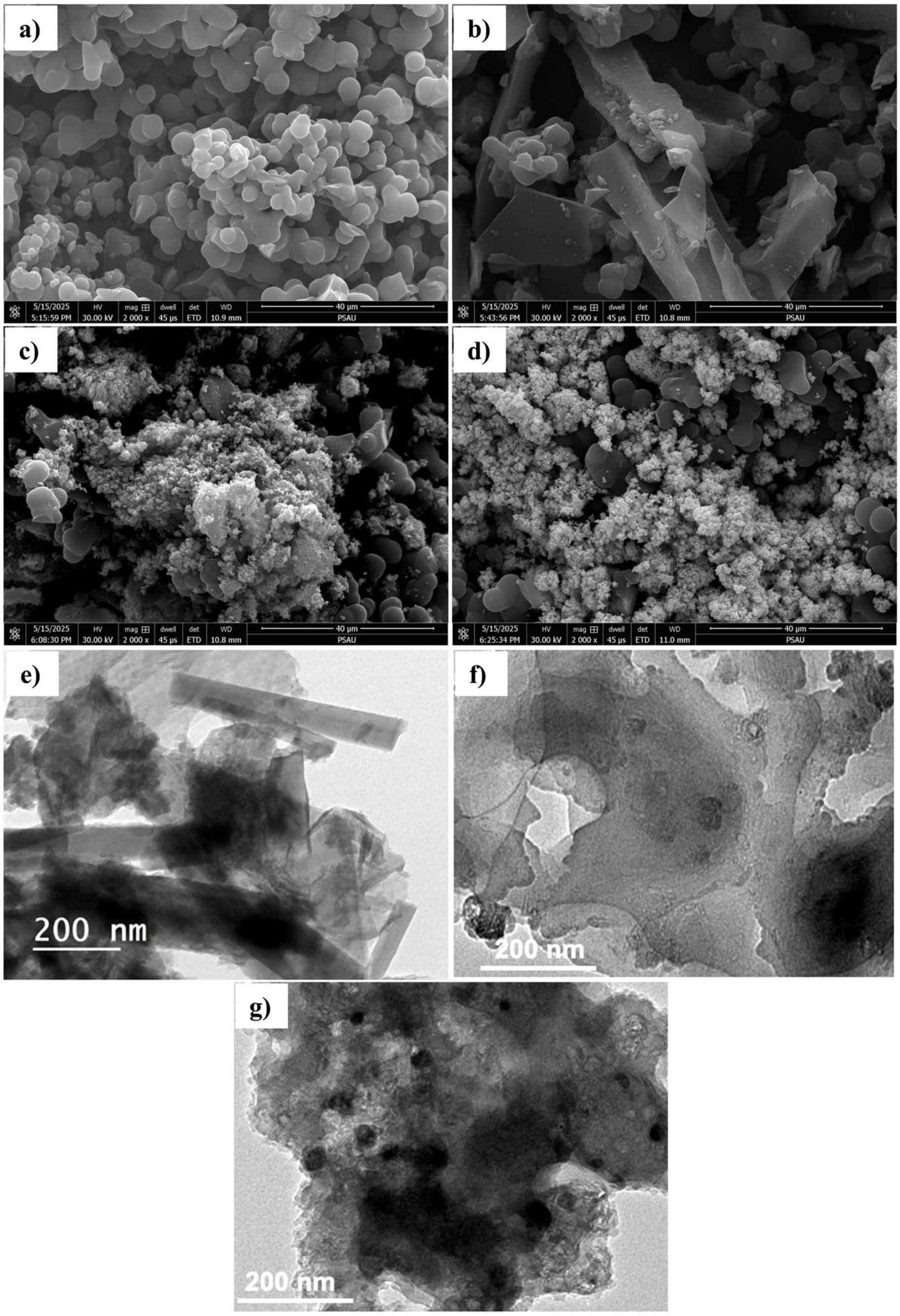

Fig. 2 FESEM images of (a) CX, (b) Pt5/CX, (c) Pt5:Ru2.5/CX, and (d) Pt5:Ru5/CX. HRTEM images of (e) Pt5/CX, (f) Pt5:Ru2.5/CX, and (g) Pt5:Ru5/CX.

mostly persisted post-Pt loading. The minor positive displacement in the primary graphitic peak (from 284.00 to 284.43 eV) indicates a potential interaction between the Pt nanoparticles and the carbon matrix, perhaps involving charge transfer from the carbon support to Pt. This interaction can improve metal dispersion and catalytic stability.

The C 1s spectra of Pt5:Ru2.5/CX, shown in Fig. 3c, exhibited three deconvoluted peaks at 284.39, 284.54, and 285.36 eV. The lack of a prominent peak above 288 eV (O–C═O) in this bimetallic system signifies a decrease in carboxylic oxygen species or a transition resulting from Ru inclusion. The diminishing energy gap between sp^2 carbon (∼284.39 eV) and oxidized carbon (∼285.36 eV) indicates a change in surface chemistry, perhaps resulting from enhanced electron density or the introduction of new chemical states by Ru. The peak at 284.54 eV may suggest the existence of C–Pt–Ru or partially hydrogenated C–C species at the metal–support interface. The C 1s peaks for Pt5:Ru5/CX, shown in Fig. 3d, were detected at 284.38, 284.88, and 285.56 eV. The graphitic carbon peak exhibited minimal variation compared to Pt5:Ru2.5/CX;

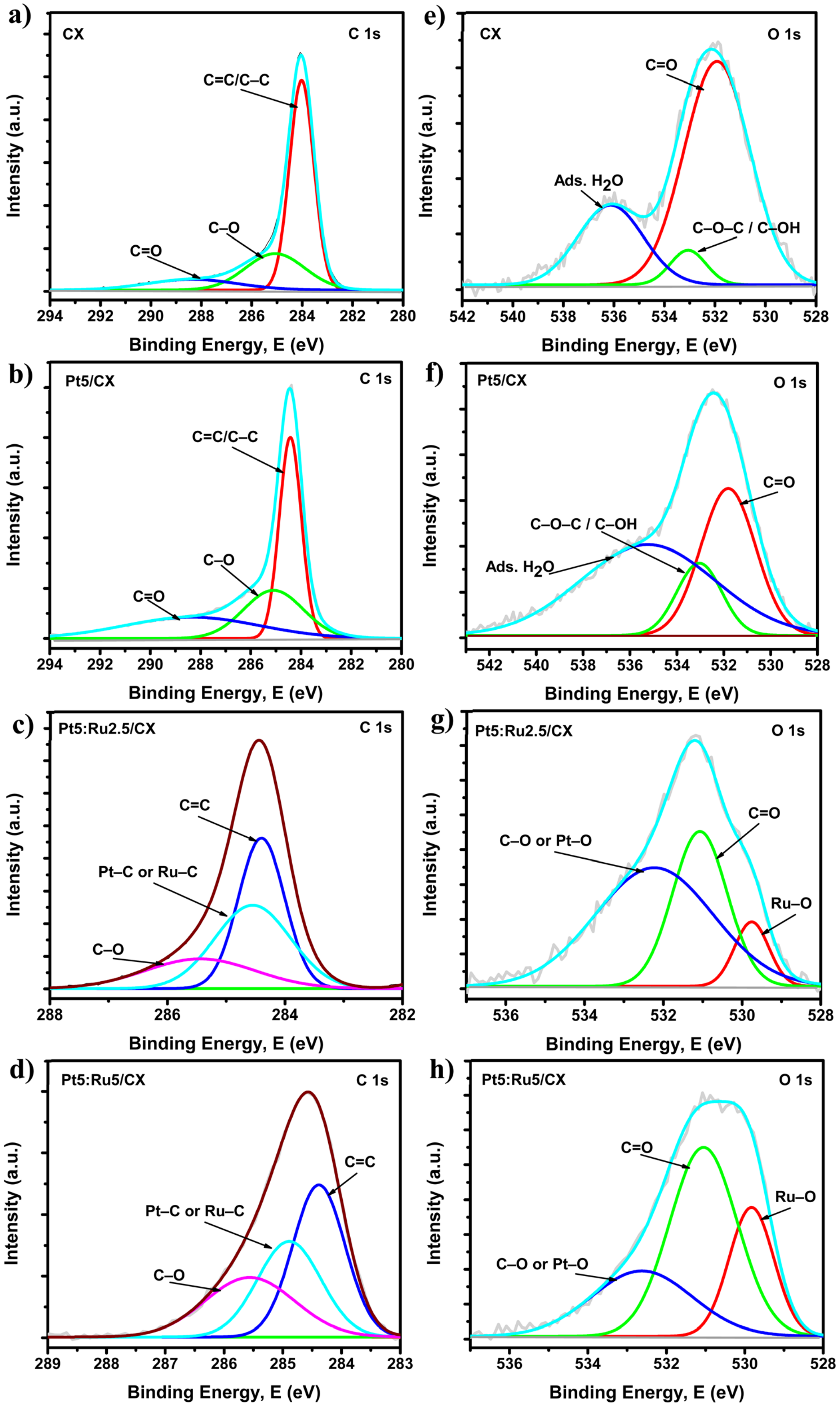

Fig. 3 XPS spectra of C 1s and O 1s for CX (a and e), Pt5/CX (b and f), Pt5:Ru2.5/CX (c and g), and Pt5:Ru5/CX (d and h).

however, the oxidized species demonstrated an additional shift towards elevated binding energy. This trend may indicate enhanced electron delocalization and intensified electronic interaction between the carbon support and the higher Ru concentration, potentially modifying the surface charge distribution. The attenuation of high-binding-energy O–C═O peaks

Table 1 The position, FWHM, and atomic% for C 1s, O 1s, Pt 4f, and Ru 3d for the prepared samples

Sample	Spectra	Position, eV	FWHM	Atomic%
CX	C 1s	284.00	1.13	92.32
		285.07	2.76	
		288.36	4.18	
	O 1s	531.92	3.07	7.68
		533.06	1.67	
		536.13	3.05	
Pt5%/CX	C 1s	284.43	1.04	81.63
		285.09	2.79	
		288.34	6.34	
	O 1s	531.80	2.75	18.37
		533.04	2.25	
		535.23	6.76	
Pt5%:Ru2.5%/CX	C 1s	284.40	0.93	79.17
		284.54	1.46	
		285.36	2.10	
	O 1s	529.73	1.03	12.30
		531.06	1.70	
		532.32	3.45	
	Pt 4f	71.51	1.15	5.46
		72.49	2.44	
		74.85	1.22	
		75.91	2.32	
	Ru 3d	280.17	0.76	3.07
		280.85	1.5	
		284.41	1.12	
		285.44	1.55	
Pt5%:Ru5%/CX	C 1s	284.38	1.05	84.24
		284.88	1.27	
		285.56	1.79	
	O 1s	529.83	1.34	7.85
		531.05	2.03	
		532.63	3.02	
	Pt 4f	71.57	1.20	3.94
		72.79	1.89	
		74.91	1.32	
		76.06	3.19	
	Ru 3d	280.16	0.92	3.97
		280.97	1.65	
		284.49	1.12	
		285.45	1.63	

further suggests that other oxygen functions may have been depleted or altered during hydrothermal reduction and alloy synthesis. The progression of the C 1s spectra among the samples indicates nuanced alterations in the surface chemistry of the CX following metal loading. These comprise minor variations in binding energy resulting from charge transfer, variations in the relative strengths of oxidized and graphitic carbon species, and a reduction or alteration of surface oxygen-containing groups in Pt–Ru bimetallic complexes.

The O 1s spectra were deconvoluted into three separate peaks for each sample, as seen in Fig. 3 and detailed in Table 1. The O 1s spectra of CX, shown in Fig. 3e, displayed three prominent peaks at 531.92 eV, 533.06 eV, and 536.13 eV. These peaks are ascribed to C=O species, C–O, and physically adsorbed water or weakly bound molecular oxygen.[24] The existence of these oxygen functionalities is essential for attaching metal ions and affecting surface hydrophilicity. In the Pt5/CX sample, as shown in Fig. 3f, the O 1s peaks were seen at 531.8, 533.04, and 535.23 eV, closely mirroring those of pristine CX. Moreover, there is a reduction of the C=O peak intensity and higher peak intensities were observed for C–O and a minor downshift for the ads. H_2O peak, suggesting higher moisture adsorption, as shown in Table 1. The broad closeness in peak positions indicates that the oxygen species were predominantly unchanged over the Pt loading process, with only slight alterations due to metal–support interactions.

The O 1s spectra of Pt5:Ru2.5/CX, as shown in Fig. 3g, exhibited notable alterations, with peaks at 529.73, 531.06, and 532.32 eV. The new low-binding-energy peak at about 529.7 eV signifies lattice oxygen in metal oxides, particularly RuO_2 or surface-attached Ru–O molecules.[16] This signal corroborates the existence of oxidized ruthenium species on the catalyst surface, aligning with the partial oxidation of Ru during preparation or XPS analysis. The second peak at approximately 531.1 eV is attributed to residual C=O species or metal–OH groups, while the third peak at around 532.3 eV belongs to adsorbed –OH or the Pt–O bond. The O 1s spectrum of Pt5:Ru5/CX, as shown in Fig. 3h, exhibited peaks at 529.83, 531.05, and 532.63 eV, which closely correspond to those of Pt5:Ru2.5/CX. The pronounced peak at around 529.8 eV further corroborates the existence of lattice oxygen linked to RuO_2 or Ru–O bonds, which intensifies with increased Ru concentration.[20] The little elevation of the third peak to 532.6 eV may result from increased surface hydroxylation or hydrogen bonding with adjacent oxygen molecules in a more oxidized environment.

The XPS spectra of Pt 4f and Ru 3d for Pt5:Ru2.5/CX and Pt5:Ru5/CX samples are shown in Fig. 4. The Pt 4f spectrum often consists of two spin–orbit doublets: Pt $4f_{7/2}$ and Pt $4f_{5/2}$, which are separated by around 3.3 to 3.4 eV.[25] Notably, although the presence of Pt was unequivocally verified by XRD and FESEM for all Pt-loaded samples, the Pt 4f signal was absent in the XPS spectrum of Pt5/CX. This disparity arises from the surface-sensitive characteristics of XPS, which examines only the upper few nanometers of the material. FESEM study indicated that Pt in Pt5/CX exhibits a tendency to form heterogeneous and partially aggregated sheet-like structures, which are likely embedded inside or partially obscured by the carbon xerogel framework. This morphology diminishes the effective surface exposure of Pt, thereby impeding its detection by XPS.[26] Conversely, the bimetallic Pt5:Ru2.5/CX and Pt5:Ru5/CX samples demonstrated uniformly disseminated Pt nanoparticles characterized by reduced dimensions and a more homogeneous surface distribution, as evidenced by FESEM images. These characteristics improved the surface accessibility of Pt and facilitated its distinct identification in the XPS Pt 4f region. The lack of Pt 4f peaks in Pt5/CX does not signify the absence of Pt; instead, it denotes variations in surface accessibility and particle morphology resulting from the catalyst's composition and structure. The Pt 4f spectrum usually exhibits two significant peaks associated with Pt^0, centered around: Pt $4f_{7/2}$ 71.1–71.5 eV and Pt $4f_{5/2}$ 74.4–74.8 eV. The subtle shoulders with marginally elevated binding energies may suggest the presence of oxidized platinum species (Pt^{2+} or Pt^{4+}), maybe resulting from surface oxidation upon exposure to air.[27] In the

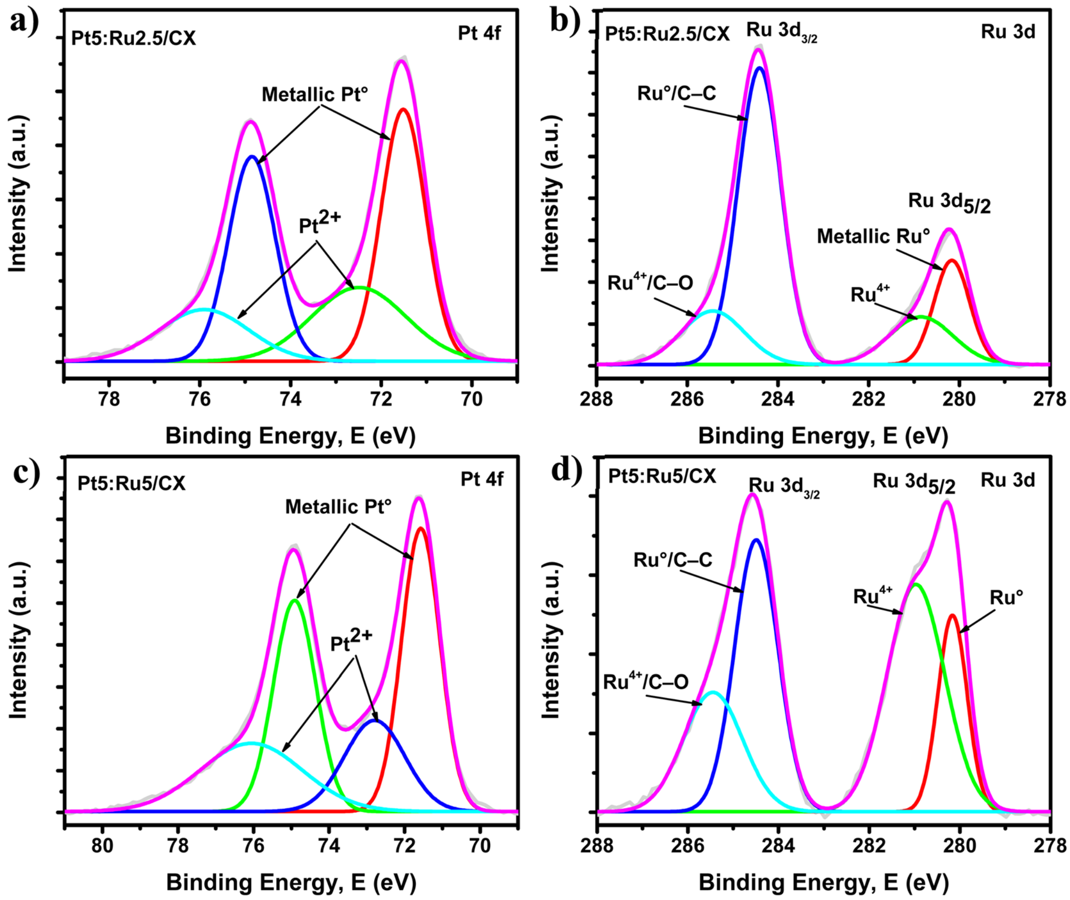

Fig. 4 High-resolution XPS spectra of (a and c) Pt 4f and (b and d) Ru 3d for Pt5:Ru2.5/CX and Pt5:Ru5/CX.

Pt5:Ru2.5/CX sample, four peaks were identified at 71.50, 72.49, 74.85, and 75.91 eV, corresponding to: Pt $4f_{7/2}$ at 71.50 eV, Pt^{2+} $4f_{7/2}$ at 72.49 eV, Pt $4f_{5/2}$ at 74.85 eV, and Pt^{2+} $4f_{5/2}$ at 75.91 eV, as shown in Fig. 4b. The results unequivocally demonstrate the existence of both metallic Pt^0 and oxidized Pt^{2+} species.[25] The partial oxidation of Pt is attributable to electronic interactions with Ru atoms or surface hydroxyl/oxide species. The presence of Pt^0 and Pt^{2+} indicates a synergistic electronic interaction between Pt and Ru, potentially altering the d-band center of Pt and enhancing hydrogen evolution reaction kinetics. The Pt5:Ru5/CX sample, as shown in Fig. 4c, displayed marginally displaced peaks at 71.57, 72.79, 74.91, and 76.06 eV, corresponding to: Pt $4f_{7/2}$ at 71.57 eV, Pt^{2+} $4f_{7/2}$ at 72.79 eV, Pt $4f_{5/2}$ at 74.91 eV and Pt^{2+} $4f_{5/2}$ at 76.06 eV. The elevation in binding energy of both Pt^0 and Pt^{2+} species relative to Pt5:Ru2.5/CX indicates a more robust Pt–Ru electrical interaction with increased Ru concentration. The upward shift can be understood as an electron-withdrawing influence of Ru, which marginally decreases the electron density on Pt atoms, rendering them more electrophilic.

The Ru 3d spectra of the bimetallic electrocatalysts were also analyzed, as shown in Fig. 4d and e. Owing to the intersection of the Ru 3d signals with the C 1s peak, meticulous deconvolution was executed to distinguish the separate contributions. The Ru 3d spectra for both Pt5:Ru2.5/CX and Pt5:Ru5/CX exhibited two unique Ru $3d_{5/2}$ features, indicative of metallic and oxidized ruthenium species, in addition to two C 1s-related peaks.[28] In Pt5:Ru2.5/CX, as shown in Fig. 4d, the Ru $3d_{5/2}$ component was seen at binding energies of 280.17 and 280.85 eV. The initial peak at 280.17 eV is ascribed to metallic Ru^0, signifying the successful integration of reduced ruthenium species into the carbon xerogel matrix.[29] The secondary signal at 280.85 eV is attributed to Ru^{4+} species, presumably in the form of RuO_2 or surface-attached Ru–O species. The findings indicate the existence of a mixed-valence state of ruthenium, wherein metallic and oxidized species coexist on the catalyst surface. This is advantageous for the hydrogen evolution reaction (HER), as Ru^0 can operate as active sites for hydrogen adsorption, whereas Ru^{4+} species are recognized for promoting water dissociation. The C 1s peaks seen at 284.41 and 285.43 eV correspond to sp^2-hybridized carbon (C–C/C=C) and oxygenated functional groups (C–O/C–OH), respectively. For Pt5:Ru5/CX, as shown in Fig. 4e, the Ru $3d_5/_2$ peaks were detected at 280.16 and 280.97 eV, further validating the presence of both Ru^0 and Ru^{4+} species. In comparison to Pt5:Ru2.5/CX, the Ru^{4+} peak in this sample demonstrated a minor shift towards elevated binding energy with higher intensities, indicating an increased level of surface oxidation or enhanced Ru–O interactions with higher Ru loading. The C 1s peaks at 284.49 and 285.45 eV were somewhat displaced, presumably owing to altered electronic

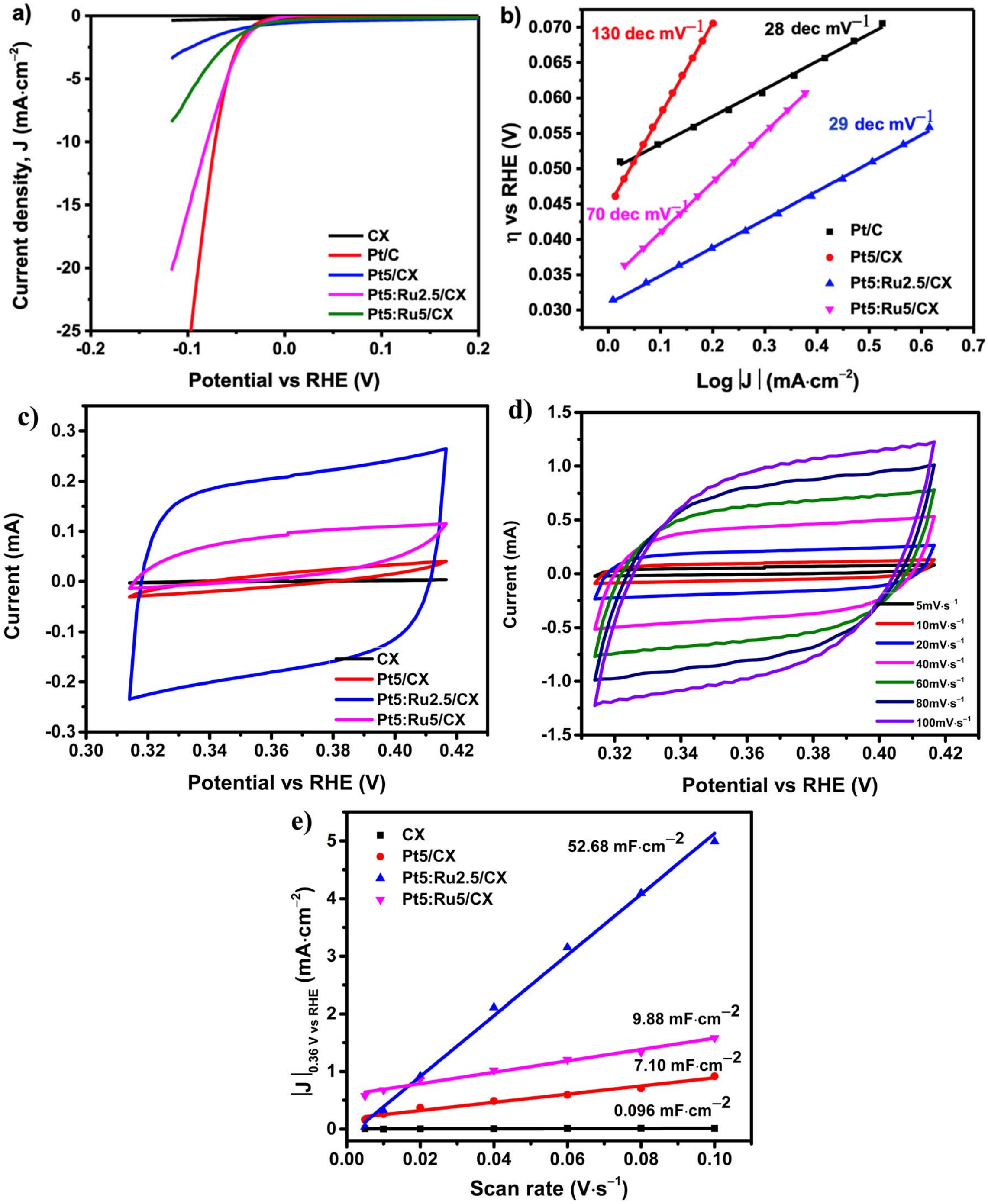

Fig. 5 (a) LSV curves for CX, Pt5/CX, Pt5:Ru2.5/CX, Pt5:Ru5/CX, and commercial Pt electrodes at a scan rate of 5 mV s^{-1} in 0.5 M H_2SO_4, (b) Tafel plots, (c) CV curves in the non-faradaic region at a scan rate of 20 mV s^{-1}, (d) CV curves of Pt5:Ru2.5/CX at different scan rates and (e) the C_{dl} values.

interactions between the carbon matrix and the predominant Ru species.

Fig. S1 shows the XPS survey spectrum of Pt5:Ru2.5/CX where the presence of C, O, Pt, and Ru was confirmed. As mentioned above, the C 1s appears at about 284.5 eV, the O 1s region appeared at about 532 eV, Pt 4f has a doublet in the region between 71 and 76 eV which is assigned to metallic Pt^0 and Pt^{2+} species, and the Ru 3d doublet at 280–281 eV overlapped with the C 1s region. Furthermore, there is a doublet for Ru $3p_{3/2}$ at about 462 eV which also confirms the coexistence of metallic Ru^0 and Ru^{4+} species on the catalytic surface.

3.2 HER activity

The activity of the produced electrocatalysts for the hydrogen evolution reaction (HER) was assessed in 0.5 M H_2SO_4 *via* linear sweep voltammetry (LSV) at a scan rate of 5 mV s^{-1}. Fig. 5a shows that the CX demonstrated the least effective HER performance, as anticipated, owing to its restricted intrinsic catalytic activity and absence of active metal sites.[5] The introduction of 5 wt% platinum (Pt5/CX) resulted in a significant improvement in HER activity, due to the presence of Pt^0 sites that promote proton reduction and hydrogen generation. Nonetheless, the overpotential and current density remained subpar in comparison to that of the bimetallic catalysts and commercial Pt/C electrode. Of the synthesized materials, the Pt5:Ru2.5/CX electrode demonstrated superior HER activity, characterized by an exceptionally low onset potential of −0.03 V *vs.* RHE and low overpotential of 39 mV at a current density of 10 mA cm^{-2}. Both Pt5:Ru2.5/CX and commercial Pt/C exhibited almost comparable onset potentials, suggesting that the incorporation of a minor quantity of Ru into the Pt-loaded carbon matrix substantially alters the electronic structure and catalytic performance of Pt. The enhanced performance is probably attributable to the synergistic interaction between Pt and Ru, with Ru aiding in water dissociation and Pt enhancing hydrogen adsorption and desorption.[10,22] Elevating the Ru concentration to 5% in Pt5:Ru5/CX resulted in a marginal decrease in performance, perhaps attributable to excessive Ru oxidation, inadequate Pt–Ru dispersion, or blocking of the CX pores.

To obtain a more profound understanding of the HER kinetics of the synthesized electrocatalysts, the Tafel slopes were extracted from the linear sweep voltammetry (LSV) curves and are illustrated in Fig. 5b. The Tafel slope indicates the rate-determining step of the reaction and elucidates the reaction process. A high Tafel slope often indicates slow kinetics, whereas a smaller value denotes accelerated charge-transfer activities.[28] The CX demonstrated a significantly elevated Tafel slope of 458 mV dec^{-1} (not seen in the figure), signifying suboptimal HER kinetics attributed to the lack of active metallic sites and sluggish proton adsorption and electron transfer processes. Conversely, Pt5/CX exhibited a markedly reduced Tafel slope of 130 mV dec^{-1}, indicating the advantageous contribution of Pt nanoparticles in augmenting HER activity. The addition of ruthenium to the Pt-based system considerably diminished the Tafel slopes: 70 mV dec^{-1} for Pt5:Ru5/CX and 29 mV dec^{-1} for Pt5:Ru2.5/CX. Significantly, Pt5:Ru2.5/CX had a Tafel slope approximately equivalent to that of commercial Pt/C (28 mV dec^{-1}), indicating comparable hydrogen evolution reaction kinetics. The significant enhancement in the Tafel slope resulting from co-loading with a little quantity of Ru (2.5%) can be ascribed to the synergistic interaction between Pt and Ru, wherein Ru facilitates water dissociation and alters the electronic structure of Pt to optimize hydrogen binding energy.[10]

Cyclic voltammetry (CV) was performed in the non-faradaic potential range to assess the double-layer capacitance (C_{dl}) for all samples, as shown in Fig. 5c. The acquired CV curves demonstrated notable disparities in double-layer charging currents, indicating discrepancies in surface area and accessibility of active sites.[30] Among the analyzed materials, the Pt5:Ru2.5/CX electrode demonstrated the maximum capacitive current, signifying the greatest double-layer capacitance, C_{dl} of 52.68 mF cm^{-2} and the most plentiful active surface sites for the HER. Pt5:Ru5/CX exhibited a substantial double-layer current, marginally inferior to that of Pt5:Ru2.5/CX, potentially due to partial surface obstruction or agglomeration at elevated Ru concentrations. Pt5/CX exhibited moderate capacitive behavior, indicative of the aggregated Pt structures. Conversely, the bare CX demonstrated the minimal charging current, underscoring its restricted surface activity without metal loading.

Fig. 5d shows the CV measurements of Pt5:Ru2.5/CX in the non-faradaic region at different scan rates. The resultant CV curves demonstrated an elevation in capacitive current with increasing scan rate, signifying characteristic electrochemical double-layer charging behavior. Fig. S2 exhibits the CV plots for CX, Pt5/CX, and Pt5:Ru5/CX at different scan rates. Additionally, the double-layer capacitance (C_{dl}) was derived from the slope of the current density against the scan rate and analyzed across all synthesized samples, as shown in Fig. 5e. The linear correlation between the current density and scan rate confirms that the

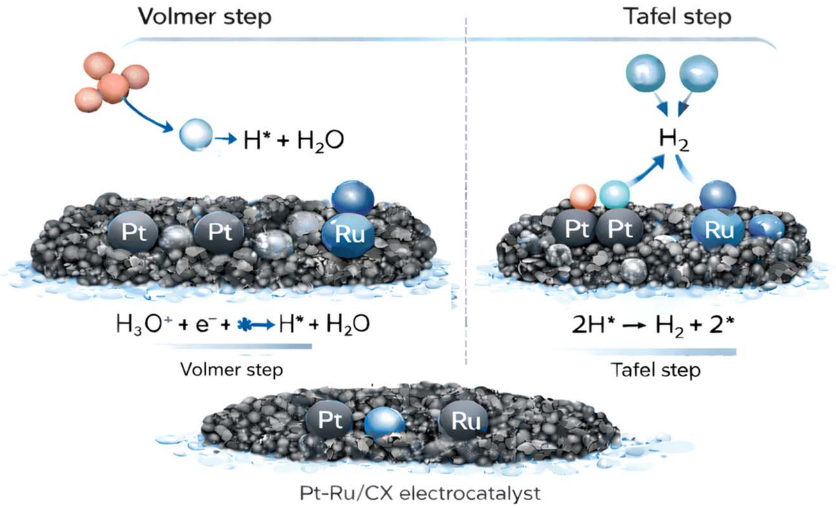

Fig. 6 The suggested mechanism for the HER over the surface of the Pt–Ru/CX electrocatalyst.

measured currents primarily resulted from double-layer charging rather than faradaic processes.[30] The C_{dl} values adhered to the following trend: CX (0.096 mF cm^{-2}) < Pt5/CX (7.10 mF cm^{-2}) < Pt5:Ru5/CX (9.88 mF cm^{-2}) < Pt5:Ru2.5/CX (52.68 mF cm^{-2}). The ECSA for the electrodes was estimated based on the measured C_{dl} values of CX, Pt5/CX, Pt5:Ru2.5/CX, and Pt5:Ru5/CX, where their corresponding ECSA is 2.4, 178, 1317, and 247 cm^2, respectively. The higher ECSA for Pt5:Ru2.5/CX signifies an optimized Pt–Ru composition, with superior dispersion, and more accessible active sites which is consistent with its superior HER activity.

Fig. 6 demonstrates the suggested mechanism for the HER over the Pt–Ru/CX electrocatalyst where the reaction proceeds through a Volmer–Tafel mechanism. In the first step protons from the hydronium ions are electrochemically discharged on the Pt–Ru/CX surface, producing adsorbed hydrogen intermediates (H*) according to the following Volmer step:

$$H_3O^+ + e^- + * \rightarrow H^* + H_2O$$

where * is the free active site on Pt–Ru/CX and the presence of Ru facilitates proton and water activation. Subsequently, the adsorbed hydrogen recombines *via* the Tafel step that produces molecular hydrogen according to the following equation:

$$2H^* \rightarrow H_2 + 2^*$$

Pt serves as the primary site for H–H recombination, while the interactions between Pt and Ru modulate the hydrogen binding energy and lower the energy barrier in the Tafel step. Moreover, the carbon xerogel support offers a 3D structure which enhances the electron transport and uniform distribution of Pt and Ru.

The turnover frequency (TOF) values were computed to assess the intrinsic catalytic activity of the synthesized materials by normalizing the hydrogen evolution rate to the quantity of active sites, as shown in Fig. 7a.[31] The CX sample demonstrated a minimal TOF of 0.25 Hz (inset of Fig. 7a), aligning with its subpar HER performance and absence of active metal sites. Upon platinum loading, Pt5/CX exhibited a significant enhancement in turnover frequency (3.6 Hz), indicating the existence of catalytically active platinum sites. An additional improvement in TOF was noted for the bimetallic samples, with Pt5:Ru5/CX exhibiting a superior TOF compared to Pt5/CX, attributed to the synergistic interaction between Pt and Ru

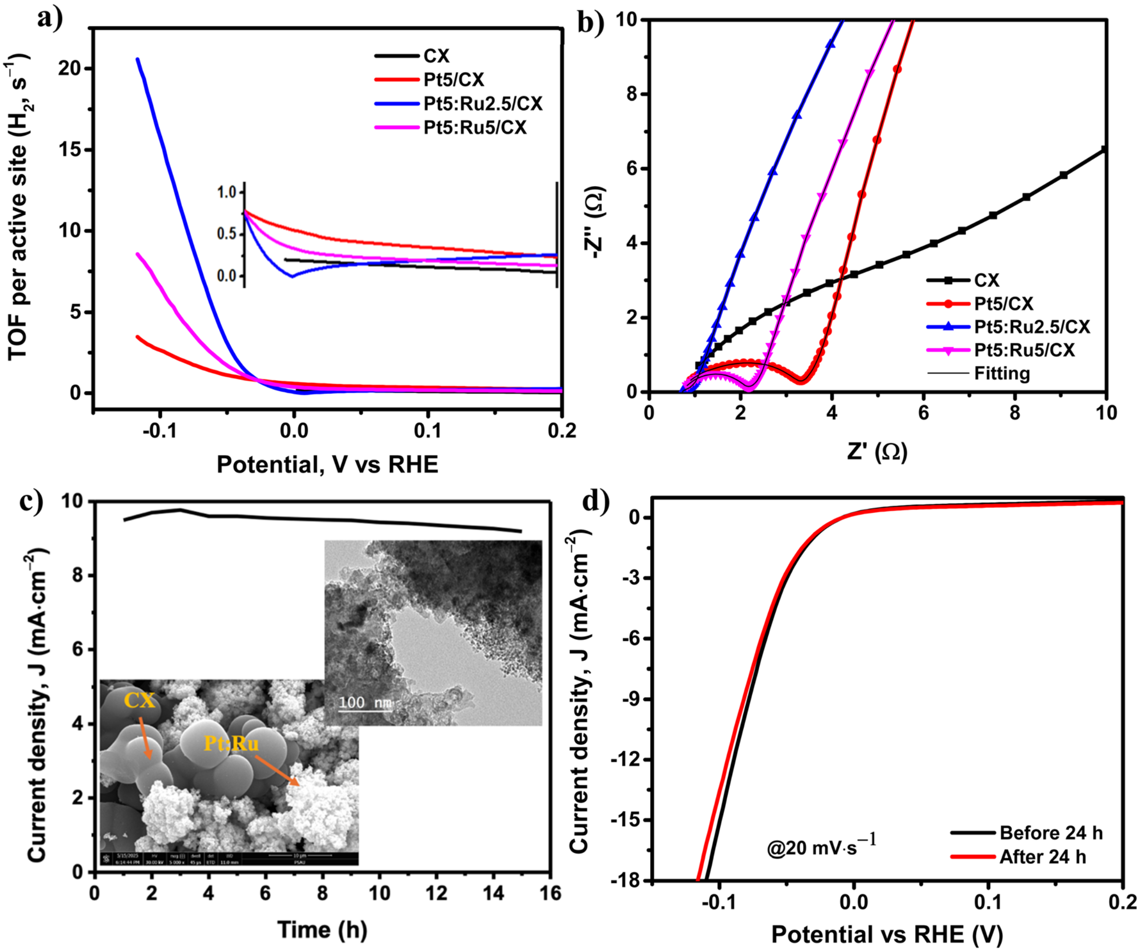

Fig. 7 (a) TOF, (b) Nyquist plots derived from EIS, (c) chrono-potentiometric stability assessment at a constant current density of 10 mA cm^{-2} for 15 h with post-FESEM and HRTEM analysis, and (d) LSV cycling at 20 mV s^{-1} for 24 hours for Pt5:Ru2.5/CX.

species that facilitates more effective water dissociation and proton reduction. Significantly, Pt5:Ru2.5/CX attained the highest TOF among all evaluated electrodes (21.6 Hz), exceeding that of Pt5:Ru5/CX, so demonstrating that the optimal Pt-to-Ru ratio at 2.5% Ru loading facilitates the most effective exploitation of active sites.[32] This trend demonstrates that both the presence and the composition and distribution of active metals significantly affect the intrinsic catalytic efficiency for the HER.

Electrochemical impedance spectroscopy (EIS) was used to assess the resistance of electrolyte (R_s), the charge transfer resistance (R_{ct}) and interfacial conductivity of the synthesized electrodes, as depicted in the Nyquist plots, shown in Fig. 7b. The Nyquist plots were fitted with a Randles-type equivalent circuit using NOVA 1.11 software. The equivalent circuit consists of solution resistance (R_s) connected in series with the charge-transfer resistance (R_{ct}) and a constant phase element (CPE_{dl}). Due to the presence of an inclined line at low frequency, then there is a contribution from the Warburg element, so the final equivalent circuit can be written as: $[R_s–(R_{ct}\|CPE_{dl})–W]$. Table 2 summarizes the data obtained from the fitting, where the CX exhibited the most extensive semicircle diameter in the high-frequency domain, signifying a high charge transfer resistance (R_{ct}) of 6.6 Ω and sluggish electron transfer kinetics.[33] The addition of 5 wt% Pt to the CX matrix (Pt5/CX) markedly diminished the semicircle diameter, indicating a lower charge transfer resistance of 2.9 Ω attributed to the presence of highly conductive Pt. Additional improvement was noted in the bimetallic catalysts, specifically Pt5:Ru2.5/CX, which had the smallest semicircle among all samples, indicating the lowest R_{ct} (0.4 Ω) and the most effective electron transport characteristics. The enhanced conductivity results from the synergistic interaction between Pt and Ru, facilitating advantageous electrical interactions and improved dispersion. In contrast, Pt5:Ru5/CX exhibited a somewhat bigger semicircle than Pt5:Ru2.5/CX (1.6 Ω), potentially attributable to high Ru content resulting in partial surface passivation or enhanced charge carrier scattering. The electrolyte resistance was measured to be 0.7 Ω, while the equivalent series resistance (ESR) values for CX, Pt5/CX, Pt5:Ru2.5/CX, and Pt5:Ru5/CX were 7.3, 3.6, 1.1, and 2.3 Ω, respectively. These results clearly indicate that Pt5:Ru2.5/CX exhibits the lowest ESR, confirming its superior electrical conductivity and more efficient charge-transport characteristics. The EIS results align closely with the changes in HER performance, underscoring the significant impact of interfacial charge transfer resistance on catalytic efficiency.

Table 2 The ECSA and EIS fitting data for the prepared electrocatalysts

Catalysts	ECSA (cm^2)	R_s (Ω)	R_{ct} (Ω)	ESR (Ω)
CX	2.4	0.7	6.6	7.3
Pt5/CX	178	0.7	2.9	3.6
Pt5:Ru2.5/CX	1317	0.7	0.4	1.1
Pt5:Ru5/CX	247	0.7	1.6	2.3

The enduring electrochemical stability of the fabricated electrodes was evaluated *via* chronopotentiometry at a constant current density of 10 mA cm^{-2} for 15 h, as shown in Fig. 7c, and repetitive linear sweep voltammetry (LSV) cycling at 20 mV s^{-1} for a duration of 24 hours, as shown in Fig. 7d. The chronopotentiometric profiles revealed that Pt5:Ru2.5/CX displayed excellent stability with a constant current response with no drift over time with a current retention of 94% after 15 h, signifying exceptional operational durability under prolonged HER conditions. In addition, post-FESEM and post-HRTEM analyses were performed, as shown in Fig. 7c, showing the morphology of Pt5:Ru2.5/CX after the long-lasting chronopotentiometry measurements for 15 h, indicating that Pt5:Ru2.5/CX maintains excellent morphological stability after prolonged electrochemical operation. Moreover, over 24 hours of repetitive LSV cycling, Pt5:Ru2.5/CX maintained almost equivalent HER activity with minimal variation in onset potential or current density, thereby affirming its substantial electrochemical stability and resilience against corrosion or active site degradation. The results underscore the structural integrity and long-term durability of the Pt5:Ru2.5/CX catalyst, positioning it as a suitable candidate for practical hydrogen evolution reaction applications. Furthermore, Table 3 presents a comparison of overpotentials and Tafel slopes for Pt5:Ru5/CX and already published studies. The Pt5:Ru5/CX catalyst in 0.5 M H_2SO_4 demonstrates a low overpotential of 39 mV at 10 mA cm^{-2} and a Tafel slope of 29 mV dec^{-1}, highlighting its superior efficiency. Comparatively, other catalysts like Pt–NiRu LDH and Pt–Ru dimers show relatively low overpotentials of 38 mV and 50 mV, respectively, but differ in electrolyte and Tafel slope values. The results suggest the potential use of Pt5:Ru2.5/CX as an electrocatalyst for the HER.

Table 3 Comparison between the electrochemical activity of the HER in this work and the published ones

Catalyst	Electrolyte	Overpotential @ 10 mA cm^{-2} (mV)	Tafel slope (mV dec^{-1})	Reference
Pt5:Ru2.5/CX	0.5 M H_2SO_4	39	29	This work
Pt–NiRu LDH	1.0 M KOH	38	39	34
Pt–Ru dimers	0.5 M H_2SO_4	50	28.9	10
g-C_3N_4@Pt	0.5 M H_2SO_4	100	77	35
Pt–C 30 wt%	0.5 M H_2SO_4	50	31.9	36
Pt–TiO_2/CC	0.5 M H_2SO_4	38	47	37
Ru–Ru_2P/2D-PCSG	0.5 M H_2SO_4	57	35	13
Ru-XC	1.0 M KOH	42	41	38

4. Conclusion

This study involved the synthesis and comprehensive investigation of platinum- and ruthenium-loaded carbon xerogel-based electrocatalysts for the hydrogen evolution reaction (HER) under acidic conditions. The inclusion of 5 wt% Pt (Pt5/CX) markedly enhanced the hydrogen evolution reaction (HER) activity relative to the unmodified carbon xerogel (CX), while the integration of Ru as a co-catalyst further augmented the performance. The Pt5:Ru2.5/CX catalyst demonstrated superior HER activity among all synthesized materials, characterized by a minimal overpotential, the lowest Tafel slope (39 mV dec^{-1}), the greatest electrochemically active surface area (ECSA), and the highest turnover frequency (TOF), comparable to those of commercial platinum. Electrochemical impedance spectroscopy validated its exceptional charge transfer characteristics, while cyclic voltammetry and chronopotentiometry assessments exhibited its remarkable electrochemical stability and longevity which confirms that the CX mitigates the Ru leaching into the liquid phase. The enhanced performance of Pt5:Ru2.5/CX is ascribed to the synergistic interaction between Pt and Ru, which optimizes hydrogen adsorption and water dissociation, while improving electron conductivity and accessibility to active sites. This study emphasizes the promise of systematically engineered bimetallic electrocatalysts, based on porous carbon matrices, as efficient and economical substitutes for high-Pt loading systems in hydrogen evolution reaction (HER) applications.

Conflicts of interest

There are no conflicts to declare.

Data availability

The data supporting this article have been included as part of the main manuscript.

Supplementary information (SI) is available. See DOI: https://doi.org/10.1039/d5na00946d.

Acknowledgements

This research has been funded by Scientific Research Deanship at the University of Hail – Saudi Arabia through project number «RG-24 023».

References

1 M. A. Abdelkareem, K. Elsaid, T. Wilberforce, M. Kamil, E. T. Sayed and A. Olabi, Environmental aspects of fuel cells: A review, *Sci. Total Environ.*, 2021, **752**, 141803, DOI: 10.1016/j.scitotenv.2020.141803.

2 A. K. Kunhiraman, T. A. Raj, M. R. Puthalath, I. Alonso-Lemus and R. Aishwarya, Pd–MoS_2/CoS_2@Carbon nanostructure as cathode catalyst for proton exchange membrane water electrolyser, *Int. J. Hydrogen Energy*, 2025, **144**, 1231–1239, DOI: 10.1016/j.ijhydene.2025.04.361.

3 I. Dincer and C. Acar, Review and evaluation of hydrogen production methods for better sustainability, *Int. J. Hydrogen Energy*, 2015, **40**(34), 11094–11111, DOI: 10.1016/j.ijhydene.2014.12.035.

4 H. Zhao, *et al.*, Key Role of Bridge Adsorbed Hydrogen Intermediate on Pt–Ru Pair for Efficient Acidic Hydrogen Production, *Adv. Mater.*, 2025, 2503221, DOI: 10.1002/adma.202503221.

5 C. Li and J.-B. Baek, Recent Advances in Noble Metal (Pt, Ru, and Ir)-Based Electrocatalysts for Efficient Hydrogen Evolution Reaction, *ACS Omega*, 2020, **5**(1), 31–40, DOI: 10.1021/acsomega.9b03550.

6 J. Durst, C. Simon, F. Hasché and H. A. Gasteiger, Hydrogen Oxidation and Evolution Reaction Kinetics on Carbon Supported Pt, Ir, Rh, and Pd Electrocatalysts in Acidic Media, *J. Electrochem. Soc.*, 2014, **162**(1), F190–F203, DOI: 10.1149/2.0981501jes.

7 G. M. Abdelrazek, M. M. El-Deeb, A. A. Farghali, A. F. Pérez-Cadenas and A. Abdelwahab, Design of Self-Supported Flexible Nanostars MFe-LDH@ Carbon Xerogel-Modified Electrode for Methanol Oxidation, *Materials*, 2021, **14**(18), 5271, DOI: 10.3390/ma14185271.

8 A. Abdelwahab, F. Carrasco-Marín and A. F. Pérez-Cadenas, Carbon Xerogels Hydrothermally Doped with Bimetal Oxides for Oxygen Reduction Reaction, *Materials*, 2019, **12**(15), 2446.

9 A. F. Pérez-Cadenas, *et al.*, Metal-doped carbon xerogels for the electro-catalytic conversion of CO_2 to hydrocarbons, *Carbon*, 2013, **56**, 324–331.

10 L. Zhang, *et al.*, Atomic layer deposited Pt-Ru dual-metal dimers and identifying their active sites for hydrogen evolution reaction, *Nat. Commun.*, 2019, **10**(1), 4936, DOI: 10.1038/s41467-019-12887-y.

11 S. E. Islam, D.-R. Hang, C.-T. Liang, K. H. Sharma, H.-C. Huang and M. M. C. Chou, Tuning the electrocatalytic activity of MoS2 nanosheets via the in situ hybridization with ruthenium and graphene network, *Chem. Eng. J.*, 2024, **488**, 150950, DOI: 10.1016/j.cej.2024.150950.

12 P. Su, *et al.*, Exceptional Electrochemical HER Performance with Enhanced Electron Transfer between Ru Nanoparticles and Single Atoms Dispersed on a Carbon Substrate, *Angew. Chem., Int. Ed.*, 2021, **60**(29), 16044–16050, DOI: 10.1002/anie.202103557.

13 L. Liu, Z. Wang, X. Zhang, L. Luo and Y. Chen, Anchoring Ru-Ru_2P heterojunction on P-doped graphene for enhanced HER performances of water electrolysis, *J. Alloys Compd.*, 2025, **1010**, 177725, DOI: 10.1016/j.jallcom.2024.177725.

14 Z. Zapata-Benabithe, F. Carrasco-Marín, J. de Vicente and C. Moreno-Castilla, Carbon xerogel microspheres and monoliths from resorcinol–formaldehyde mixtures with varying dilution ratios: preparation, surface characteristics, and electrochemical double-layer capacitances, *Langmuir*, 2013, **29**(20), 6166–6173.

15 F. Wu, Y. Liu and C. Wu, Nanostructure and formation mechanism of Pt-WO_3/C nanocatalyst by ethylene glycol

method, *J. Wuhan Univ. Technol., Mater. Sci. Ed.*, 2011, **26**(3), 377–383, DOI: 10.1007/s11595-011-0233-1.

16 A. Abdelwahab, J. R. Humaidi, F. Abdulaziz, A. Alanazi and K. M. Alenezi, Evaluating the role of SnSe on the catalytic activity of co-loaded carbon xerogel for hydrogen evolution reaction, *Int. J. Hydrogen Energy*, 2025, **135**, 213–220, DOI: 10.1016/j.ijhydene.2025.05.068.

17 A. Abdelwahab, J. R. Humaidi, F. Abdulaziz, A. Alanazi and K. M. Alenezi, Tailoring MoS_2 nanosheets dispersion on carbon xerogel with carbon quantum dots for efficient hydrogen evolution reaction, *Int. J. Hydrogen Energy*, 2025, **179**, 151750, DOI: 10.1016/j.ijhydene.2025.151750.

18 M. A. Wasfey, A. Abdelwahab, F. Carrasco-Marín, A. F. Pérez-Cadenas, H. H. Abdullah, I. S. Yahia and A. A. Farghali, Nickel Cobaltite Functionalized Silver Doped Carbon Xerogels as Efficient Electrode Materials for High Performance Symmetric Supercapacitor, *Materials*, 2020, **13**(21), 4906.

19 S.-S. Chen, X.-X. Lin, A.-J. Wang, H. Huang and J.-J. Feng, Facile synthesis of multi-branched AgPt alloyed nanoflowers and their excellent applications in surface enhanced Raman scattering, *Sens. Actuators, B*, 2017, **248**, 214–222, DOI: 10.1016/j.snb.2017.03.129.

20 Q. Wang, *et al.*, Trace Pt Induced electron-enriched Ru to boost interfacial water-activation for alkaline hydrogen generation under industrial condition, *Chem. Eng. J.*, 2025, **512**, 162421, DOI: 10.1016/j.cej.2025.162421.

21 X. Xu, J. Zhu, J. L. Faria, J. Li and J. L. Figueiredo, Tuning the textural and surface properties of carbon xerogels to be used as supports for gold catalysts, *Cent. Eur. J. Chem.*, 2012, **10**(6), 1867–1874.

22 D. Zhang, *et al.*, Noble Metal (Pt, Rh, Pd, Ir) Doped Ru/CNT Ultra-Small Alloy for Acidic Hydrogen Evolution at High Current Density, *Small*, 2022, **18**(3), 2104559, DOI: 10.1002/smll.202104559.

23 X. Chen, X. Wang and D. Fang, A review on C1s XPS-spectra for some kinds of carbon materials, *Fullerenes, Nanotubes Carbon Nanostruct.*, 2020, **28**(12), 1048–1058, DOI: 10.1080/1536383X.2020.1794851.

24 T. Yamashita and P. Hayes, Analysis of XPS spectra of Fe^{2+} and Fe^{3+} ions in oxide materials, *Appl. Surf. Sci.*, 2008, **254**(8), 2441–2449, DOI: 10.1016/j.apsusc.2007.09.063.

25 M.-J. Choi, H. Park, M. H. Engelhard, D. Li, P. V. Sushko and Y. Du, Reevaluation of XPS Pt 4f peak fitting: Ti 3s plasmon peak interference and Pt metallic peak asymmetry in Pt@TiO_2 system, *J. Vac. Sci. Technol., A*, 2024, **42**(6), 063209, DOI: 10.1116/6.0003973.

26 N. Fairley, P. Bargiela and J. Baltrusaitis, Surface analysis insight note: Illustrating the effect of adventitious contamination on Pt photoemission peak intensities, *Surf. Interface Anal.*, 2024, **56**(2), 122–125, DOI: 10.1002/sia.7276.

27 E. I. Vovk, A. V. Kalinkin, M. Yu. Smirnov, I. O. Klembovskii and V. I. Bukhtiyarov, XPS Study of Stability and Reactivity of Oxidized Pt Nanoparticles Supported on TiO_2, *J. Phys. Chem. C*, 2017, **121**(32), 17297–17304, DOI: 10.1021/acs.jpcc.7b04569.

28 J. Liu, *et al.*, Ru-triggered domino effect constructs a local acid-like environment to achieve the ampere-level current density of a/c-Ru-FeP/IF electrode for alkaline HER, *Appl. Catal., B*, 2025, **366**, 125030, DOI: 10.1016/j.apcatb.2025.125030.

29 D. J. Morgan, Resolving ruthenium: XPS studies of common ruthenium materials, *Surf. Interface Anal.*, 2015, **47**(11), 1072–1079, DOI: 10.1002/sia.5852.

30 Z. Huang, J. Li, S. Guo, J. Liu, J. Zeng and F. Yuan, Polyacrylonitrile-based 3D N-rich activated porous carbon synergized with Co-doped MoS_2 for promoted electrocatalytichydrogenevolution, *Sep. Purif. Technol.*, 2025, **354**, 129011, DOI: 10.1016/j.seppur.2024.129011.

31 S. Anantharaj, P. E. Karthik and S. Noda, The Significance of Properly Reporting Turnover Frequency in Electrocatalysis Research, *Angew. Chem., Int. Ed.*, 2021, **60**(43), 23051–23067, DOI: 10.1002/anie.202110352.

32 W.-C. Hsu and Y.-H. Wang, Homogeneous Water Oxidation Catalyzed by First-Row Transition Metal Complexes: Unveiling the Relationship between Turnover Frequency and Reaction Overpotential, *ChemSusChem*, 2022, **15**(5), e202102378, DOI: 10.1002/cssc.202102378.

33 A. Abdelwahab, J. Castelo-Quibén, M. Pérez-Cadenas, F. J. Maldonado-Hódar, F. Carrasco-Marín and A. F. Pérez-Cadenas, Insight of the effect of graphitic cluster in the performance of carbon aerogels doped with nickel as electrodes for supercapacitors, *Carbon*, 2018, **139**, 888–895, DOI: 10.1016/j.carbon.2018.07.034.

34 D. Li, *et al.*, An effective hybrid electrocatalyst for the alkaline HER: Highly dispersed Pt sites immobilized by a functionalized NiRu-hydroxide, *Appl. Catal., B*, 2020, **269**, 118824, DOI: 10.1016/j.apcatb.2020.118824.

35 A. Sharma, H. Devnani, J. P. Singh, M. Varshney and H. J. Shin, Synthesis of Ag and Pt-loaded g-C_3N_4 nanocomposite catalysts for improved Hydrogen evolution reaction, *Curr. Appl. Phys.*, 2025, **77**, 39–45, DOI: 10.1016/j.cap.2025.05.013.

36 A. Alsuhile, *et al.*, Synthesis of Pt Carbon Aerogel Electrocatalysts with Multiscale Porosity Derived from Cellulose and Chitosan Biopolymer Aerogels via Supercritical Deposition for Hydrogen Evolution Reaction, *Adv. Energy Sustainability Res.*, 2025, **6**(8), 2400433, DOI: 10.1002/aesr.202400433.

37 S. Wang, *et al.*, Pt nanoparticles supported on in-situ growth titanium dioxide nanowire arrays with oxygen vacancies for hydrogen evolution reaction, *Appl. Surf. Sci.*, 2025, **687**, 162257, DOI: 10.1016/j.apsusc.2024.162257.

38 H. Hu, *et al.*, p-d orbital coupling and interfacial water regulation synergistically promote alkaline hydrogen electrocatalysis on Ru/VC heterostructures, *Chem. Eng. J.*, 2025, **522**, 167317, DOI: 10.1016/j.cej.2025.167317.